doi:10.3772/j.issn.1006-6748.2018.01.008

Effect and sensitivity analysis of the rotational speed on the fluid-induced force characteristics of the straight-through labyrinth gas seal①

Wang Qingfeng(王庆峰)②*,**, He Lidong*,**
(*Beijing Key Laboratory of Health Monitoring and Self-Recovery for High-End Mechanical Equipment, Beijing University of Chemical Technology, Beijing 100029, P. R. China)
(**College of Mechanical and Electrical Engineering, Beijing University of Chemical Technology, Beijing 100029, P. R. China)

Abstract

The effects of the rotational speed on the fluid-induced force characteristics of a straight-through labyrinth gas seal (STLGS) are numerically investigated using the steady computational fluid dynamics (CFD) method based on a three-dimensional model of the STLGS. The fluid-induced force characteristics of the STLGS for five rotational speeds at a pressure drop of $\triangle P$ = 5000 Pa with and without eccentricity are computed. The grid density analysis ensures the accuracy of the present steady-CFD method. The effect and sensitivity analysis show that the changes in rotational speed affect the pressure forces, viscous forces and total pressure distributions on the rotor surface, velocity streamlines, leakage flow rates, and maximum flow velocities. The results indicate that the rotational speed inhibits the pressure forces, leakage flow rates and maximum flow velocities and promotes the viscous forces and total pressure on the rotor surface.

Key words: labyrinth seal, fluid-induced force, rotational speed, computational fluid dynamics (CFD), sensitivity analysis

0 Introduction

The labyrinth seal in turbomachinery is a key element to restrict leakage flow among rotor-stator clearances from high-pressure regions to low-pressure regions[1]. The labyrinth seal is composed of a series of circular blades and annular grooves, which present a tortuous path for the flow of the process fluid. Its overall performance affects the aerodynamic efficiency of the turbomachinery, rotor stability and operational safety[2]. The current trend in the high-performance turbomachine design requires more compact and higher-power machines with higher efficiencies because of the demand for higher rotor speeds and tighter clearances, which determines the rotor critical speeds, vibration levels, and onset of turbomachine instability[3] more accurately. Numerous experimental investigations and field troubleshooting experiences have confirmed that labyrinth seals are a major source of destabilizing forces, which result in rotordynamic instability problems, and the positive cross-coupling stiffness is the major mechanism of inducing a destabilizing force[4-6]. The pressure-driven flow in the seals can generate fluid-induced forces that become significant in some cases; thus, this flow strongly affects the overall dynamic characteristics of the machine[7]. Because these seal forces can stabilize or destabilize the rotor system and affect the vibration response of modern turbomachinery, they must be controlled to ensure that the rotor system of the turbomachinery remains stable throughout its operational duration[8]. Thus, the fluid-induced forces on the rotor from seals during machine operation must be accurately quantified to effectively predict their dynamic behavior.

To better understand the flow characteristics and improve the design performance in labyrinth seals, three main methods are most widely used in the available publications: experimental method[9], mathematical computation method[10,11], and numerical simulation method[12-15]. With the computational fluid dynamics (CFD) program, the numerical simulation method has been conducted on the leakage flow and rotordynamic characteristics of labyrinth seals. Moore[12] used three-dimensional CFD to model the labyrinth seal flow path by solving the Reynolds-Averaged Navier Stokes

① Supported by the National Basic Research Development Program of China (No. 2012CB026006).
② To whom correspondence should be addressed. E-mail: wangqf@mail.buct.edu.cn
Received on Feb. 23, 2017

equations. Unlike bulk-flow techniques, CFD makes no fundamental assumptions on the geometry, shear stress at the walls, or internal flow structure. The method enables the modeling of any arbitrarily shaped domain, including stepped and interlocking labyrinths with straight or angled teeth. The results demonstrate the improved leakage and rotordynamic prediction over bulk-flow approaches compared with experimental measurements. Hirano, et al.[13] calculated the rotordynamic force of a labyrinth seal using a commercial CFD program and further compared those results with an existing bulk flow computer program, which is currently used by major US machinery manufacturers. The leakage flow and rotor dynamics force predicted by CFX TASCFlow were compared with the results of the existing bulk flow analysis. The results show that the bulk flow program provides an overpessimistic prediction of the destabilizing forces for the conditions under investigation. Pugachev, et al.[14] proposed the CFD-based modeling of short labyrinth gas seals. The seal leakage performance can be reliably predicted with CFD for a wide operating range and various sealing configurations. However, the prediction of the seal effect on the rotordynamic stability is a challenging task that requires high computer processing power relatively. Untaroiu, et al.[15] presented a method to the linearized rotordynamic coefficients for a seal with a large aspect ratio, which uses a three-dimensional CFD analysis to predict the fluid-induced forces that act on the rotor. Although these methods are computationally efficient and can predict the dynamic properties fairly well for short seals, they lack accuracy for the seals with complex geometry or large aspect ratios. The main disadvantage of this method is the large computational time and effort required to perform the CFD analysis compared to the bulk flow analysis, which is frequently used for the lateral rotordynamic stability analysis in the industry.

Although many studies have been performed to investigate the rotordynamic coefficients of the labyrinth seal, the fluid-induced force characteristics of labyrinth seals are not fully understood. For example, the detailed insight into the effects of the rotational speed on the fluid-induced force characteristics and corresponding disciplines must be further studied[16,17]. Li, et al.[16] investigated the effects of the rotational speed on the leakage flow and cavity pressure characteristics of the rotating staggered labyrinth seal using experimental measurements and numerical simulations. The effect of the rotational speed on the leakage flow coefficient is not obvious in the present rotational speed limitations. Li, et al.[17] researched the effects of the rotational speed on the leakage and rotordynamic characteristics of a pocket damper seal using the proposed three-dimensional transient CFD. An increasing rotational speed results in a significant decrease in the effective damping term because of the obvious increase in magnitude of the destabilizing and cross-coupling stiffness with increasing rotational speed.

To obtain the fluid-induced force characteristics of labyrinth seals, the present study applies the steady-CFD method based on the three-dimensional model of STLGS. To investigate the effects of the rotational speed, computations for the fluid-induced force characteristics of the STLGS are performed for five rotational speeds at a pressure drop of $\triangle P = 5000$Pa with and without eccentricity. The primary objective of this work is to numerically study the effect and sensibility of rotational speed on the fluid-induced force characteristics of the STLGS.

1 Method

1.1 Computational model and numerical method

According to the conventional straight-through labyrinth seal, the geometry of the STLGS is shown as Fig. 1. Table 1 provides the detailed geometrical dimensions of STLGS.

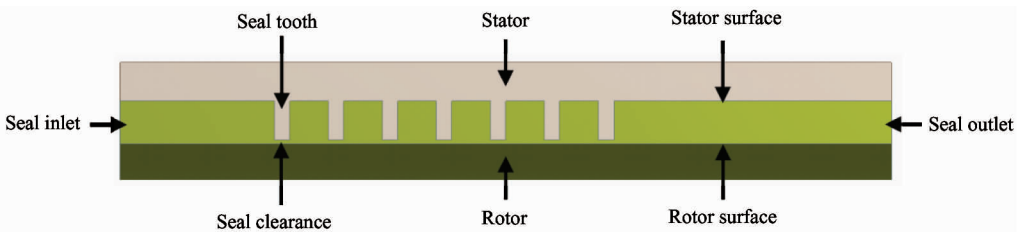

Fig. 1 Geometry of the STLGS

Table 1 Geometrical dimensions

Parameter	Value
Seal length (m)	0.1
Seal inlet length (m)	0.02
Seal clearance (m)	0.0005
Seal tooth height (m)	0.005
Seal tooth width (m)	0.002
Seal tooth pitch (m)	0.005
Rotor diameter (m)	0.05
Tooth number	7

Fig. 2 shows the computational model and mesh of the STLGS. Because the geometry of the STLGS is non-axisymmetric and the circumferential fluid-induced forces in the whirling STLGS are non-uniform, a three-dimensional computational model with or without eccentricity is required to obtain the flow characteristics using the steady CFD. In this work, the commercial software ANSYS DesignModeler 17.0 and ANSYS ICEM CFD 17.0 are used to generate the three-dimensional computational model and unstructured mesh for the calculations, respectively.

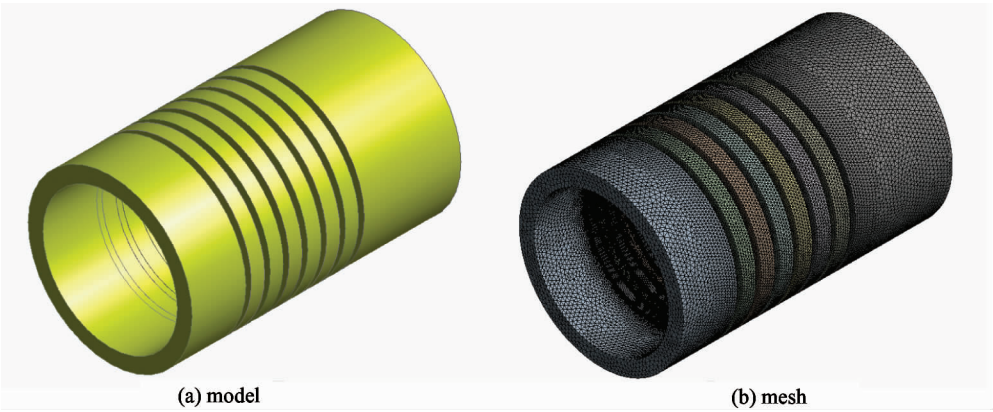

Fig. 2 Computational model and mesh of the STLGS

In this work, the fluid-induced force characteristics are numerically predicted for STLGS using the steady-CFD method based on three-dimensional models. The present steady-CFD analyses are conducted using the commercial software ANSYS-CFX 17.0 to solve the imcompressible Reynolds-averaged Navier-Stokes equations. Table 2 lists the detailed numerical approaches for the steady-CFD analyses and parameters. The shear stress transport model accounts for the transport of the turbulent shear stress and provides highly accurate predictions of the onset and amount of flow separation under adverse pressure gradients. The shear stress transport model is applied to model the turbulence characteristics of the flow. The high-resolution scheme is applied for the advection scheme and turbulence numerics. Based on the past CFD analyses and computational convergence[12-15], the flow regime (subsonic), opening pressure (relative pressure), flow direction (normal to the boundary condition), and turbulence quantities (turbulence intensity = 5%) are defined for the seal inlet and outlet boundaries. The inlet pre-swirl velocity is considered negligible.

Table 2 Numerical parameters

Solution type	Steady
Fluid	Air at 25℃
Computational method	Time marching method
Turbulence model	Shear stress transport
Wall properties	Adiabatic, smooth surface
Advection scheme	High resolution
Turbulence numerics	High resolution
Minimum number of iterations	1
Maximum number of iterations	300
Residual type	RMS
Residual target	1E-04

To obtain the fluid-induced force characteristics, calculation with a whirling rotor is necessary, where the rotor whirls and spins around the center of the seal stator and rotor, respectively. In a stationary frame of reference, the geometry of the rotor appears to be moving, so the moving grid and transient analysis are necessary. However, in a rotating frame of reference, the rotor always remains fixed, and the analysis becomes steady-state. Hence, the rotating reference frame with ω is selected in this work. In the rotating reference frame, it is assumed that the speeds of the seal rotor and seal fluid are ω, the axis of the rotating reference frame is the axis of the seal rotor, and the seal fluid is eccentric.

1.2 Computational mesh analysis

To determine the necessary mesh density to accurately predict the flow characteristics of the STLGS, a mesh analysis is performed. The geometrical parameters and boundary conditions are shown in Tables 1 and 3. In the analysis, the inlet pressure and outlet pressure are 1000000 Pa and 0 Pa. Fifteen cases are selected and computed for three types of relevance center (fine, medium, coarse) and five types of relevance (0, 25, 50, 75, 100), as shown in Table 4 and Fig. 3.

Table 3 Boundary conditions

Parameter	Value
Inlet	Inlet total pressure (stable)
Outlet	Opening Pressure and Direction
Seal wall	no slip wall
Rotor wall	Angular velocity 500 rad/s

Table 4 Computational mesh cases

Case	Relevance center	Relevance	Elements	Nodes	Element quality	Flow maximum velocity (m/s)	Calculation time
1	fine	100	8074830	1819843	0.84842	842.968	2:58:30
2	fine	75	5214780	1253127	0.84708	817.919	1:48:08
3	fine	50	3701077	931874	0.83957	805.722	1:19:10
4	fine	25	2901343	742264	0.83637	791.245	1:05:14
5	fine	0	2151825	537440	0.83607	779.675	0:45:26
6	medium	100	3898392	836179	0.84373	810.302	1:53:01
7	medium	75	2543286	579878	0.84051	793.127	0:59:45
8	medium	50	1775126	416442	0.83298	775.661	0:41:29
9	medium	25	1315503	312911	0.8262	768.879	0:28:32
10	medium	0	983394	238422	0.82406	760.101	0:25:13
11	coarse	100	1233406	260444	0.83974	647.298	0:36:47
12	coarse	75	804191	178762	0.83634	637.292	0:19:19
13	coarse	50	547104	127120	0.82567	626.946	0:14:30
14	coarse	25	415359	95974	0.82014	605.591	0:09:30
15	coarse	0	334872	79204	0.81303	594.809	0:07:53

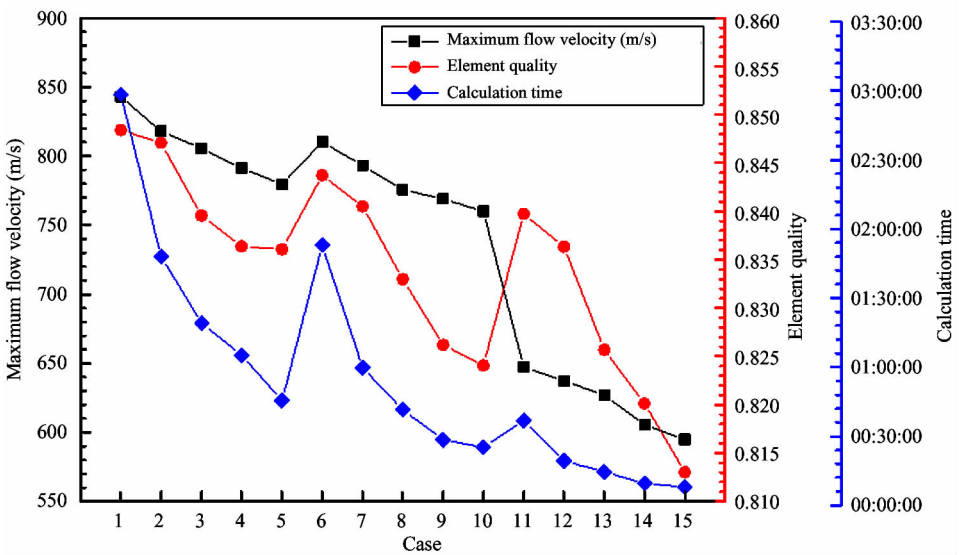

Fig. 3 Computational mesh analysis

According to the accuracy and speed of the calculations, the mesh in case 7 is selected for subsequent computations of the STLGS. In case 7, there are 2.5433×10^6 elements and 5.7988×10^5 nodes; the sizes of the mini-

mum element, maximum face element, and maximum tetrahedron element are 2.2757×10^{-5} m, 2.2757×10^{-3} m and 4.5515×10^{-3} m, respectively.

1.3 Numerical research approach

In this work, the fluid-induced force characteristics of STLGS consist of pressure forces on the rotor surface, viscous forces on the rotor surface, total pressure distributions on the rotor surface, velocity streamlines, leakage flow rates, and flow maximum velocities. The pressure force and viscous force are affected by the seal flow field on the rotor surface. The pressure force results from the pressures on the rotor surface. In this study, the pressure forces on the rotor surface consist of the radial pressure force, axial pressure force and total pressure force. The radial pressure force results from the pressure components in the X and Y directions; the axial pressure force results from the pressure component in the Z direction; the total pressure force is the sum of the pressure components in the X, Y and Z directions, all of which are numerically calculated. The viscous force results from the shear forces on the rotor surface. In this study, the viscous forces on rotor surface consist of the radial viscous force, axial viscous force and total viscous force. The radial viscous force includes the viscous force components in the X and Y directions; the axial viscous force is the viscous force component in the Z direction; the total viscous force results from the viscous force components in the X, Y and Z directions, all of which are numerically calculated.

To investigate the effects of rotational speed on the fluid-induced force characteristics of the STLGS, in this work, the computations are performed for five rotational speeds ($\omega = 200$, 275, 350, 425, 500 rad/s) at pressure drop $\triangle P = 5000$Pa (inlet pressure $= 5000$Pa; outlet pressure $= 0$Pa) without eccentricity ($e = 0.0000$m) and with eccentricity ($e = 0.0002$m). The geometrical dimensions, numerical parameters and boundary conditions of the STLGS are shown in Tables 1 – 3. Based on the computation results, the change rates of the pressure forces on the rotor surface, viscous forces on the rotor surface, leakage flow rates, and flow maximum velocities are calculated. The change rate, which is the variation-to-initial-value ratio of the fluid-induced force characteristics, reflects the effect of the rotational speed on the fluid-induced force characteristics. Finally, the sensitivity coefficients are calculated. The sensitivity coefficient is the ratio of the change rate of the fluid-induced force characteristics to the change rate of the rotational speed, particularly for monotone increasing curves or monotone decreasing curves, which is an important index to reflect the sensitivity of the rotational speed on the fluid-induced force characteristics. In this paper, the change rate and sensitivity coefficient are introduced to better understand the effect of the rotational speed on the fluid-induced force characteristics of the STLGS.

2 Results and discussion

2.1 Pressure forces on rotor surface

To investigate the effects of rotational speed on the fluid-induced force characteristics of STLGS, pressure forces, viscous forces and total pressure distributions on the rotor surface, velocity streamlines, leakage flow rates, and flow maximum velocities are computed.

Fig. 4 and Table 4 illustrate the dependence of the pressure forces on rotor surface for all five rotational speeds at $\triangle P = 5000$Pa without eccentricity ($e = 0.0000$m). The radial pressure force first increases by approximately 25.24% (from 0.00078069N at 200rad/s to 0.00097777N at 275rad/s) and subsequently decreases by approximately 30.70% (from 0.00097777N at 275rad/s to 0.00067756N at 500rad/s) with the increasing rotational speed; the maximum radial pressure forces is 0.00097777N at 275rad/s (no sensitivity). The axial pressure force decreases by approximately 0.20% (from 0.0052557N at 200 rad/s to 0.0052454N at 500rad/s) with the increasing rotational speed (sensitivity coefficient = −0.0013). The total pressure force first increases by approximately 0.59% (from 0.0053134N at 200rad/s to 0.0053447N at 275rad/s) and subsequently decreases by approximately 1.04% (from 0.0053447N at 275rad/s to 0.005289N at 500rad/s) with the increasing rotational speed; the maximum total pressure force is 0.0053447N at 275rad/s (no sensitivity). Therefore, the radial pressure force is significantly smaller than the axial pressure force, which is the crucial part of the total pressure force, and the axial pressure force is more sensitive to the increasing rotational speed.

Fig. 5 and Table 5 illustrate the dependence of the pressure forces on the rotor surface for all five rotational speeds at $\triangle P = 5000$Pa with eccentricity ($e = 0.0002$m). The radial pressure force and total pressure force first increase, subsequently decrease, and then increase with the increasing rotational speed. A peak at $\omega = 275$rad/s and a valley at $\omega = 425$rad/s (no sensitivity) appear, the total pressure force increases approximately 16.82% from 0.091086N at 200rad/s to 0.10641N at 500rad/s, the axial pressure force decreases approximately 0.27% from 0.0052452N at 200rad/s to 0.005231N at 500rad/s with the increas-

ing rotational speed, and the radial pressure force increases approximately 16.87% from 0.090935N at 200rad/s to 0.10628N at 500rad/s (sensitivity coefficient = −0.1125). Therefore, the radial pressure force is far larger than the axial pressure force, the radial pressure force is the crucial part of the total pressure force, and the axial pressure force is more sensitive to the increasing rotational speed.

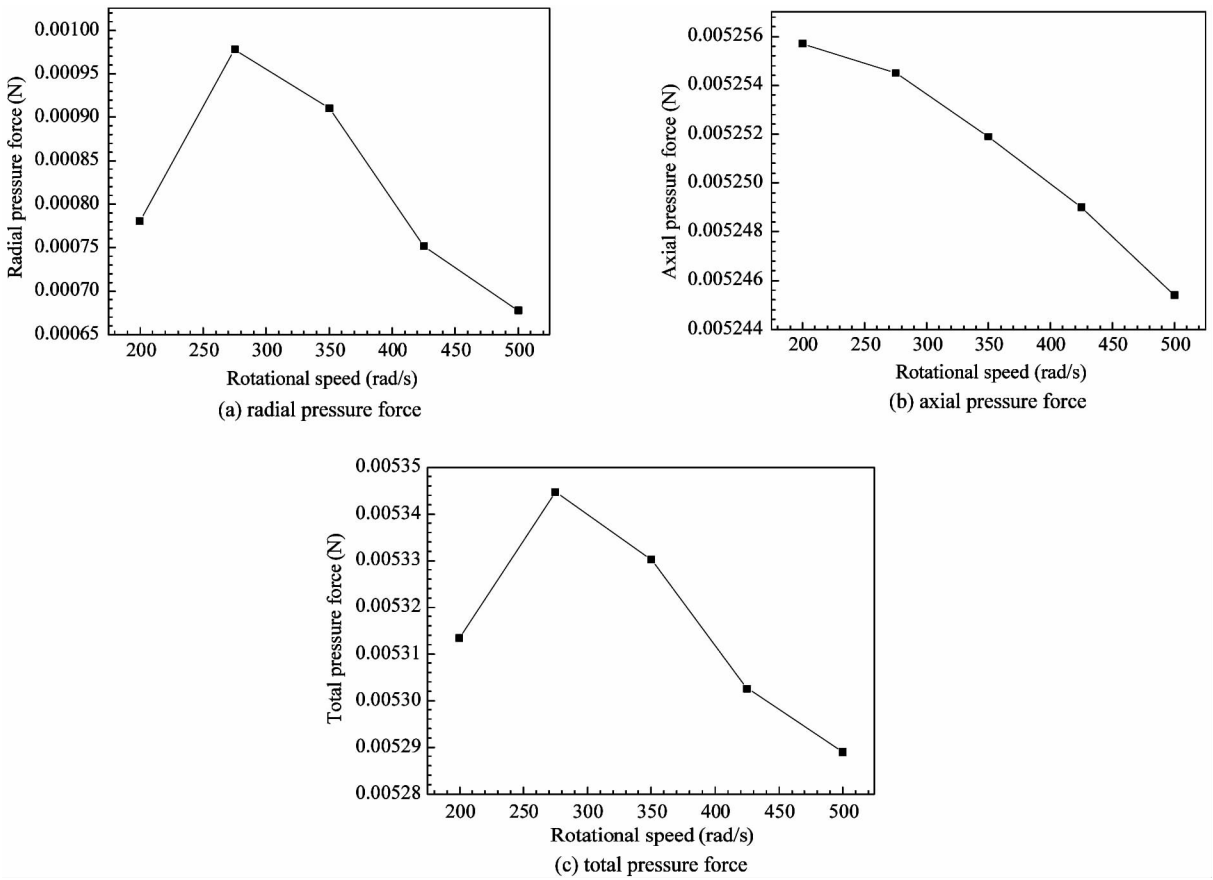

Fig. 4 Pressure forces versus rotational speed at $\triangle P = 5000$Pa without eccentricity ($e = 0.0000$m)

Table 4 Pressure forces at five rotational speeds and $\triangle P = 5000$Pa without eccentricity ($e = 0.0000$m)

Rotational speed ω (rad/s)	Radial pressure force (N)	Axial pressure force (N)	Total pressure force (N)
200	7.8069×10^{-4}	5.2557×10^{-3}	5.3134×10^{-3}
275	9.7777×10^{-4}	5.2545×10^{-3}	5.3447×10^{-3}
350	9.1048×10^{-4}	5.2519×10^{-3}	5.3302×10^{-3}
425	7.5185×10^{-4}	5.2490×10^{-3}	5.3026×10^{-3}
500	6.7756×10^{-4}	5.2454×10^{-3}	5.2890×10^{-3}

The comparison of pressure force plots in Figs 4 and 5 suggests that the radial pressure force with eccentricity is much larger than that without eccentricity, the axial pressure force with eccentricity is slightly smaller than that without eccentricity, the axial pressure force with eccentricity is more sensitive to the increasing rotational speed than that without eccentricity, and the axial pressure force with eccentricity decreases faster than that without eccentricity.

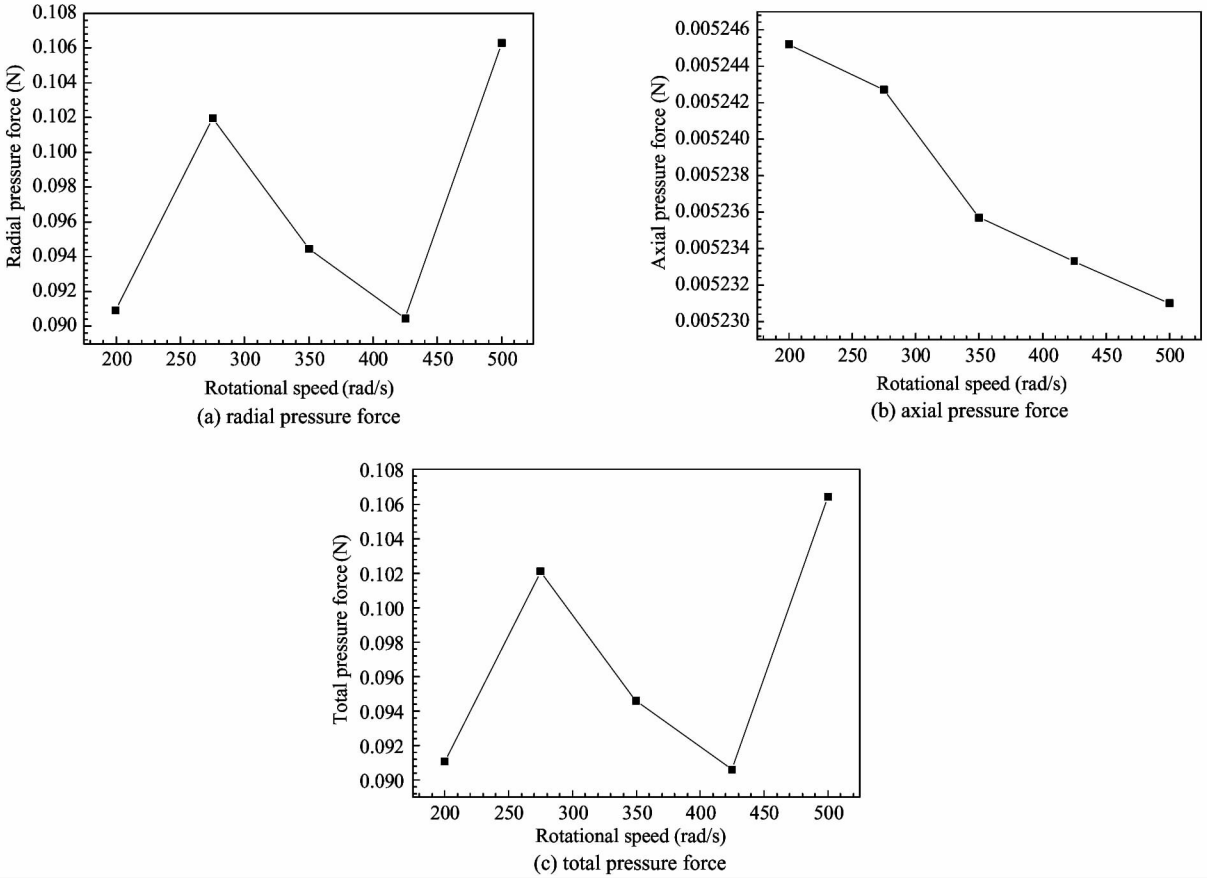

Fig. 5 Pressure forces versus rotational speed at $\triangle P = 5000$Pa with eccentricity ($e = 0.0002$m)

Table 5 Pressure forces at five rotational speeds and $\triangle P = 5000$Pa with eccentricity ($e = 0.0002$m)

Rotational speed ω(rad/s)	Radial pressure force (N)	Axial pressure force (N)	Total pressure force (N)
200	9.0935×10^{-2}	5.2452×10^{-3}	9.1086×10^{-2}
275	1.0197×10^{-1}	5.2427×10^{-3}	1.0210×10^{-1}
350	9.4444×10^{-2}	5.2357×10^{-3}	9.4589×10^{-2}
425	9.0458×10^{-2}	5.2333×10^{-3}	9.0609×10^{-2}
500	1.0628×10^{-1}	5.2310×10^{-3}	1.0641×10^{-1}

2.2 Viscous forces on the rotor surface

Fig. 6 and Table 6 illustrate the dependence of the viscous forces on the rotor surface for all five rotational speeds at $\triangle P = 5000$Pa without eccentricity ($e = 0.0000$m). The radial viscous force increases by approximately 0.27% (from 0.0000027237N at 200 rad/s to 0.000015222N at 500rad/s) with the increasing rotational speed (sensitivity coefficient = 0.0018). The axial viscous force and total viscous force increase by approximately 2.03% (from 0.087941N at 200rad/s to 0.089724N at 500rad/s) with the increasing rotational speed (sensitivity coefficient = 0.0135). Therefore, the radial viscous force is significantly smaller than the axial viscous force, the axial viscous force is the crucial part of the total viscous force, the viscous forces are sensitive to the increasing rotational speed, and the axial and total viscous forces are more sensitive than the radial viscous force.

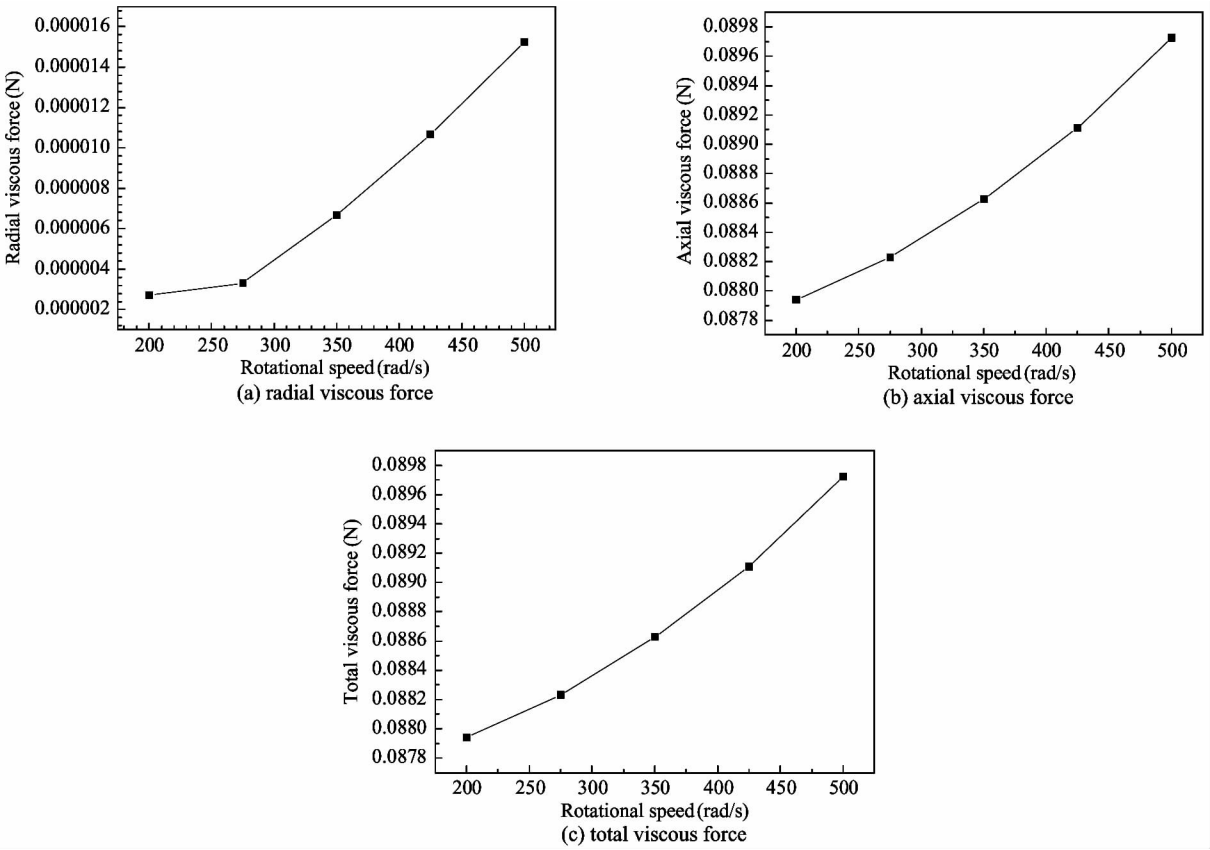

Fig. 6 Viscous forces versus rotational speed at $\triangle P = 5000$Pa without eccentricity ($e = 0.0000$m)

Table 6 Viscous forces at five rotational speeds and $\triangle P = 5000$Pa without eccentricity ($e = 0.0000$m)

Rotational speed ω (rad/s)	Radial viscous force (N)	Axial viscous force (N)	Total viscous force (N)
200	2.7237×10^{-6}	8.7941×10^{-2}	8.7941×10^{-2}
275	3.3057×10^{-6}	8.8230×10^{-2}	8.8230×10^{-2}
350	6.6762×10^{-6}	8.8628×10^{-2}	8.8628×10^{-2}
425	1.0667×10^{-6}	8.9109×10^{-2}	8.9109×10^{-2}
500	1.5222×10^{-6}	8.9724×10^{-2}	8.9724×10^{-2}

Fig. 7 and Table 7 illustrate the dependence of the seal viscous forces on the rotor surface for all five rotational speeds at $\triangle P = 5000$Pa with eccentricity ($e = 0.0002$m). The radial viscous force increases by approximately 40.79% (from 0.0013805N at 200rad/s to 0.0019436N at 500rad/s) with the increasing rotational speed (sensitivity coefficient = 0.2719). The axial viscous force increases by approximately 2.11% (from 0.086628N at 200rad/s to 0.088454N at 500rad/s) with the increasing rotational speed (sensitivity coefficient = 0.01406). The total viscous force increases by approximately 2.12% (from 0.086639N at 200rad/s to 0.088475N at 500rad/s) with the increasing rotational speed (sensitivity coefficient = 0.01413). Therefore, the radial viscous force increases more than the axial viscous force, the axial viscous force is the crucial part of the total viscous force, the viscous forces are sensitive to the increasing rotational speed, and the radial viscous force is more sensitive than the axial and total viscous forces.

The comparison of viscous forces in Figs 6 and 7 suggests that the radial viscous force with eccentricity is much larger than that without eccentricity, the axial viscous force with eccentricity is slightly smaller than that without eccentricity, the radial viscous force with eccentricity is more sensitive to the increasing rotational speed than that without eccentricity, the radial viscous force with eccentricity decreases faster than that without eccentricity, and the axial and total viscous forces with eccentricity are slightly more sensitive to the increasing rotational speed than those without eccentricity.

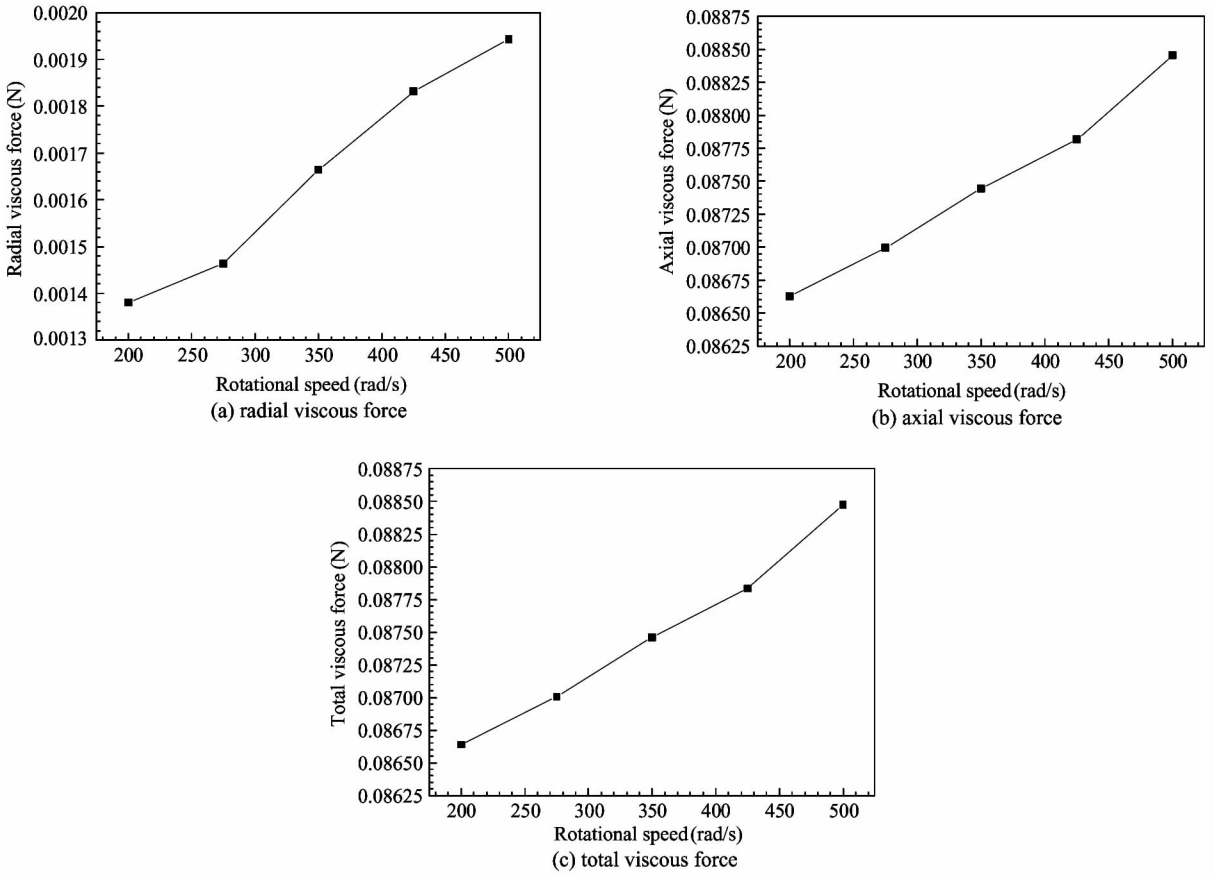

Fig. 7 Viscous forces versus rotational speed at $\triangle P = 5000\text{Pa}$ with eccentricity ($e = 0.0002\text{m}$)

Table 7 Viscous forces at five rotational speeds and $\triangle P = 5000\text{Pa}$ with eccentricity ($e = 0.0002\text{m}$)

Rotational speed ω (rad/s)	Radial viscous force (N)	Axial viscous force (N)	Total viscous force (N)
200	1.3805×10^{-3}	8.6628×10^{-2}	8.6639×10^{-2}
275	1.4643×10^{-3}	8.6994×10^{-2}	8.7006×10^{-2}
350	1.6641×10^{-3}	8.7444×10^{-2}	8.7460×10^{-2}
425	1.8311×10^{-3}	8.7816×10^{-2}	8.7835×10^{-2}
500	1.9436×10^{-3}	8.8454×10^{-2}	8.8475×10^{-2}

2.3 Total pressure distribution on the rotor surface

Fig. 8 and Fig. 9 show the total pressure contour distribution on the rotor surface through the seal at different rotational speeds and $\triangle P = 5000\text{Pa}$ for $e = 0.0000\text{m}$ and $e = 0.0002\text{m}$, respectively. As shown in Figs 8 and 9, the pressure drop from the seal inlet to the outlet is 5000Pa, and the total pressure on the rotor surface gradually decreases through the seal and with the increase in rotational speed. The comparison of the total pressure contour distribution in Figs 8 and 9 suggests that the pressure distributions on the rotor surface gradually change from axisymmetric to non-axisymmetric with increasing eccentricity.

2.4 Velocity streamlines

Fig. 10 shows the velocity streamlines through the seal at $\omega = 500\text{rad/s}$ and $\triangle P = 5000\text{Pa}$ for $e = 0.0000\text{m}$ and $e = 0.0002\text{m}$. The velocity streamlines in the seal revolve around the rotor, those in the grooves of the seal have the secondary circulation flow, and those in the outlet of the seal with eccentricity have the eccentric circulation vortex compared to those without eccentricity.

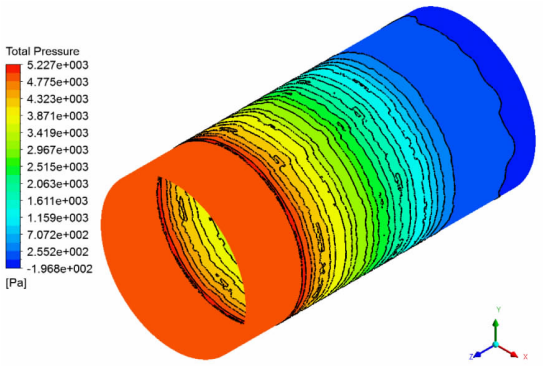

(a) 200rad/s

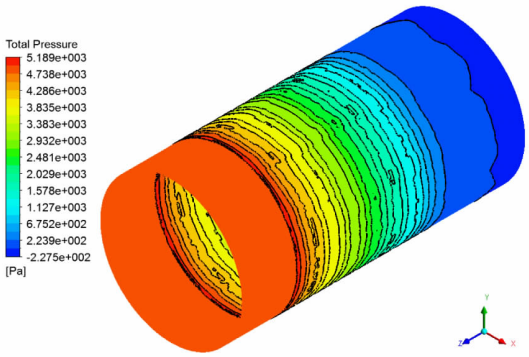

(b) 350rad/s

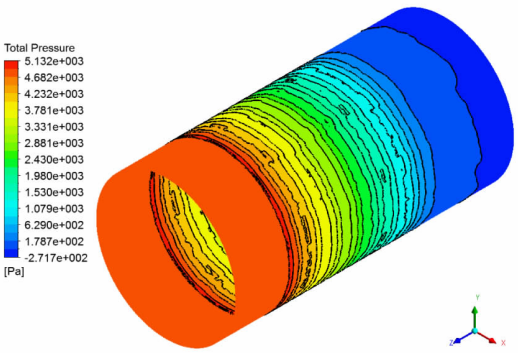

(c) 500rad/s

Fig. 8 Total pressure contours on the rotor surface at different rotational speeds ($e = 0.0000$m, $\triangle P = 5000$Pa)

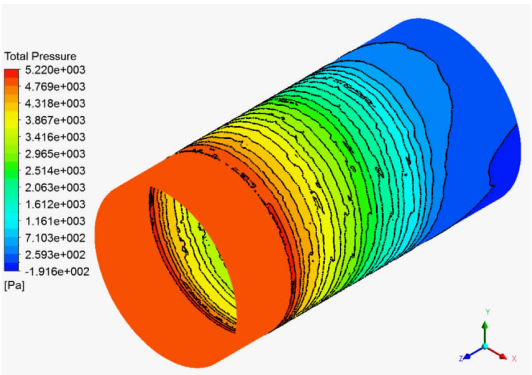

(a) 200rad/s

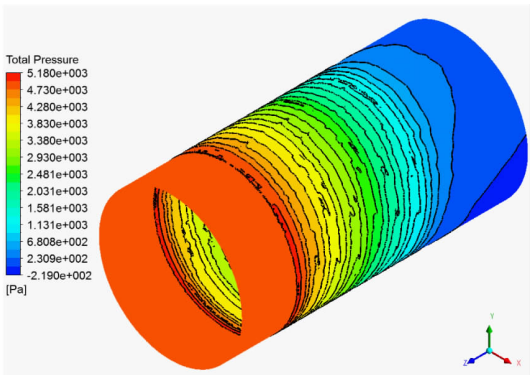

(b) 350rad/s

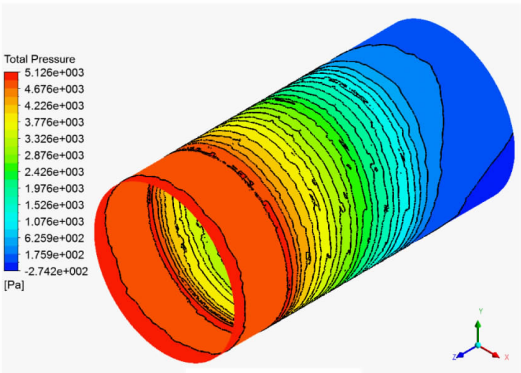

(c) 500rad/s

Fig. 9 Total pressure contours on the rotor surface at different rotational speeds ($e = 0.0002$m, $\triangle P = 5000$Pa)

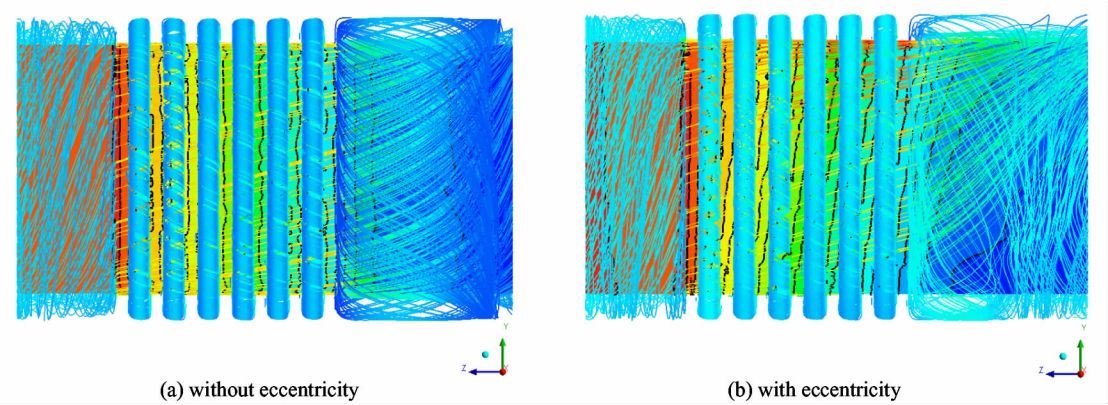

Fig. 10 Velocity streamlines at $\omega = 500$rad/s and $\triangle P = 5000$Pa

2.5 Leakage flow rate

Fig. 11 and Table 8 illustrate the dependence of the leakage flow rates for all five rotational speeds at $\triangle P = 5000$ Pa without eccentricity ($e = 0.0000$m) and with eccentricity ($e = 0.0002$m). The leakage flow rate without eccentricity decreases by approximately 0.80% (from 0.0037844kg/s at 200rad/s to 0.003754kg/s at 500rad/s) with the increasing rotational speed (sensitivity coefficient = −0.0053). The leakage flow rate with eccentricity decreases by approximately 0.74% (from 0.0038655kg/s at 200rad/s to 0.0038369kg/s at 500rad/s) with the increasing rotational speed (sensitivity coefficient = −0.0049). Therefore, the leakage flow rate with eccentricity is slightly larger than that without eccentricity, but the leakage flow rate without eccentricity is more sensitive to the increasing rotational speed and decreases faster than that with eccentricity.

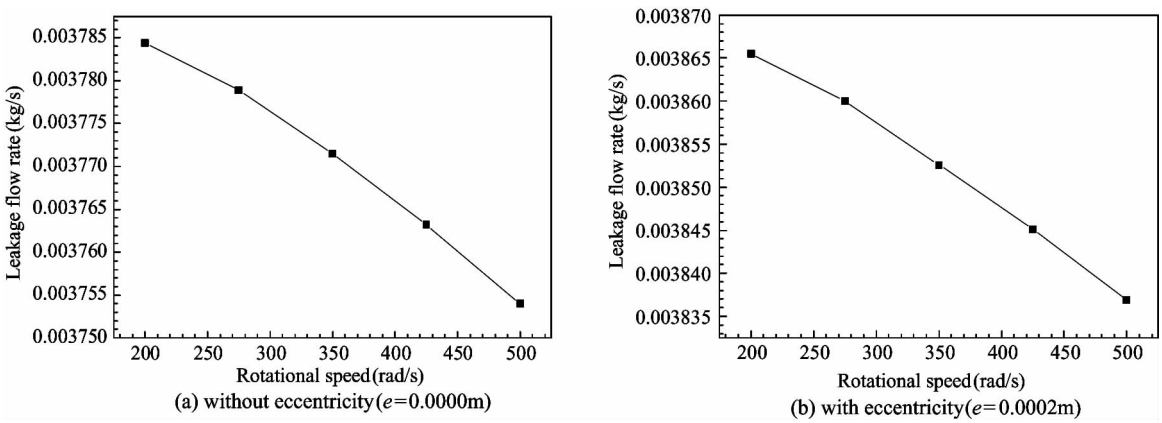

Fig. 11 Leakage flow rate versus rotational speed at $\triangle P = 5000$Pa

Table 8 Leakage flow rate at five rotational speeds and $\triangle P = 5000$Pa without eccentricity ($e = 0.0000$m) and with eccentricity ($e = 0.0002$m)

Rotational speed ω(rad/s)	Leakage flow rate (kg/s)	
	without eccentricity ($e = 0.0000$m)	with eccentricity ($e = 0.0002$m)
200	3.7844×10^{-3}	3.8655×10^{-3}
275	3.7789×10^{-3}	3.8600×10^{-3}
350	3.7715×10^{-3}	3.8526×10^{-3}
425	3.7632×10^{-3}	3.8451×10^{-3}
500	3.7540×10^{-3}	3.8369×10^{-3}

2.6 Flow maximum velocity

Fig. 12 and Table 9 illustrate the dependence of the flow maximum velocities for all five rotational speeds at $\triangle P = 5000$Pa without eccentricity ($e = 0.0000$m) and with eccentricity ($e = 0.0002$m). The flow maximum velocity without eccentricity decreases by approximately 0.93% (from 48.601m/s at 200rad/s to 48.149m/s at 500rad/s) with the increasing rota-

tional speed (sensitivity coefficient = −0.0062). The flow maximum velocity with eccentricity decreases by approximately 0.66% (from 54.34m/s at 200rad/s to 53.981m/s at 500rad/s) with the increasing rotational speed (sensitivity coefficient = −0.0044). Therefore, the flow maximum velocity with eccentricity is larger than that without eccentricity, but the flow maximum velocity without eccentricity is more sensitive to the increasing rotational speed and decreases slightly faster than that with eccentricity. The flow maximum velocity appears at the first tooth clearance at the seal inlet.

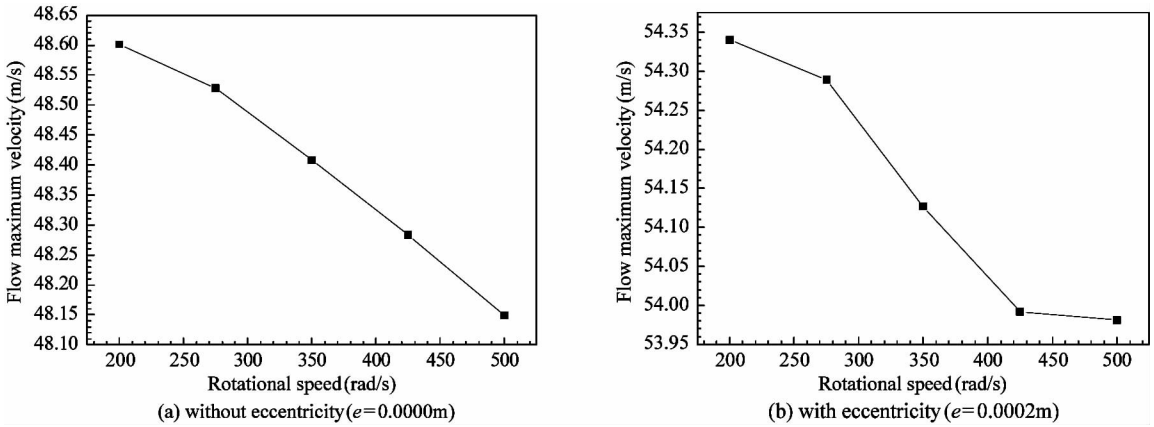

Fig. 12 Flow maximum velocity versus rotational speed at $\triangle P = 5000$Pa

Table 9 Flow maximum velocity at five rotational speeds and $\triangle P = 5000$Pa without eccentricity ($e = 0.0000$m) and with eccentricity ($e = 0.0002$m)

Rotational speed ω(rad/s)	Flow maximum velocity (m/s)	
	without eccentricity ($e = 0.0000$m)	with eccentricity ($e = 0.0002$m)
200	48.601	54.340
275	48.528	54.289
350	48.409	54.127
425	48.283	53.992
500	48.149	53.981

3 Conclusion

The fluid-induced force characteristics of STLGS, which include the pressure forces on the rotor wall, viscous forces on the rotor surface, total pressure distributions on the rotor surface, velocity streamlines, leakage flow rates, and flow maximum velocities, are numerically predicted for five rotational speeds at $\triangle P =$ 5000Pa with and without eccentricity using the steady-CFD method based on the three-dimensional models of the STLGS. The mesh density analysis ensures the accuracy of the present steady-CFD method. Several conclusions can be formulated for the STLGS in this paper by analyzing the effect of the rotational speed on the fluid-induced force characteristics.

The axial pressure force is sensitive to the rotational speed and decreases with the increasing rotational speed, but the radial pressure force and total pressure are not sensitive to the increasing rotational speed. Regardless of whether or not eccentricity is present, all viscous forces are sensitive to the rotational speed and increase with the increasing rotational speed. The eccentricity makes the radial forces increase significantly, decreases the axial forces, and changes the crucial part of the total pressure force, but does not change the crucial part of the total viscous force. The eccentricity increases the sensitivity of the axial pressure force and all viscous force to the increasing rotational speed; the sensitivity of the radial viscous force is increased more than those of the axial viscous force and total viscous force.

The change in total pressures on the rotor surface and velocity streamlines with the increasing rotational speed illustrates the change of the seal flow field. The eccentricity significantly changes the total pressures on the rotor surface and the velocity streamlines. The leakage flow rate and flow maximum velocity decrease with the increasing rotational speed, and the eccentricity increases the leakage flow rate and flow maximum

velocity.

The rotational speed inhibits the pressure forces, leakage flow rates and flow maximum velocities and promotes the viscous forces, but the change rate and sensitivity coefficient are not large. The rotational speed affects the fluid-induced force characteristics of the STLGS, particularly for high-speed turbomachinery, but the eccentricity affects the fluid-induced force characteristics of the STLGS more strongly than the rotational speed.

Conclusions of this paper will help to better understand the fluid-induced force characteristic rules of labyrinth seals by providing helpful suggestions for engineering practices and the theoretical basis to analyze the fluid-structure interaction of the seal-rotor system in future research.

References

[1] Schobeiri M. Turbomachinery Flow Physics and Dynamic Performance[M]. Berlin: Springer-Verlag, 2005. 1-12

[2] Flitney R. Seals and Sealing Handbook[M]. Amsterdam: Elsevier, 2014. 244-257

[3] Vance J M. Machinery Vibration and Rotordynamics [M]. New York: Wiley, 2010. 271-278

[4] Soto E A, Childs D W. Experimental rotordynamic coefficient results for (a) a labyrinth seal with and without shunt injection and (b) a honeycomb seal[J]. *Journal of Engineering for Gas Turbines and Power*, 1999, 121(1): 153-159

[5] Li J, Qiu B, Feng Z P. Experimental and numerical investigations on the leakage flow characteristics of the labyrinth brush seal[J]. *Journal of Engineering for Gas Turbines and Power*, 2012, 134(10): 102509

[6] Vannini G, Bertoneri M, Nielsen K K, et al. Experimental results and computational fluid dynamics simulations of labyrinth and pocket damper seals for wet gas compression [J]. *Journal of Engineering for Gas Turbines and Power*, 2015, 138(5): 052501

[7] Muszynska A. Rotordynamics[M]. Boca Raton: CRC Press/Taylor & Francis Group, 2005. 209-222

[8] Muszynska A, Bently D E. Anti-swirl arrangements prevent rotor/seal instability[J]. *Journal of Vibration, Acoustics, Stress, and Reliability in Design*, 1989, 111 (2):156-162

[9] Vance J M, Li J. Test results of a new damper seal for vibration reduction in turbomachinery[J]. *Journal of Engineering for Gas Turbines and Power*, 1996, 118(4):843-846

[10] Arghir M, Freêne J. A quasi-two-dimensional method for the rotordynamic analysis of centered labyrinth liquid seals[J]. *Journal of Engineering for Gas Turbines and Power*, 1999, 121(1): 144-152

[11] Thorat M R, Childs D W. Predicted rotordynamic behavior of a labyrinth seal as rotor surface speed approaches mach 1[J]. *Journal of Engineering for Gas Turbines and Power*, 2010, 132(11): 112504

[12] Moore J J. Three-dimensional CFD rotordynamic analysis of gas Labyrinth seals[J]. *Journal of Vibration and Acoustics*, 2003, 125(4): 427-433

[13] Hirano T, Guo Z, Kirk R G. Application of computational fluid dynamics analysis for rotating machinery—part II labyrinth seal analysis[J]. *Journal of Engineering for Gas Turbines and Power*, 2005, 127(4): 820-826

[14] Pugachev A O, Kleinhans U, Gaszner M. Prediction of rotordynamic coefficients for short labyrinth gas seals using computational fluid dynamics[J]. *Journal of Engineering for Gas Turbines and Power*, 2012, 134(6): 062501

[15] Untaroiu A, Untaroiu C, Wood H G, et al. Numerical modeling of fluid-induced rotordynamic forces in seals with large aspect ratios[J]. *Journal of Engineering for Gas Turbines and Power*, 2012, 135(1): 012501

[16] Li Z G, Li J, Yan X, et al. Effects of pressure ratio and rotational speed on leakage flow and cavity pressure in the staggered labyrinth seal[J]. *Journal of Engineering for Gas Turbines and Power*, 2011,133(11): 114503

[17] Li Z G, Li J, Yan X, et al. Numerical investigations on the leakage and rotordynamic characteristics of pocket damper seals—part I: effects of pressure ratio, rotational speed, and inlet preswirl[J]. *Journal of Engineering for Gas Turbines and Power*, 2014, 137(3): 032503

Wang Qingfeng, born in 1977. Now he is a teacher in College of Mechanical and Electrical Engineering, Beijing University of Chemical Technology. He received his M. S. E. degree from Beijing University of Chemical Technology in 2008 and his M. Sc. degree from Institute of Psychology of Chinese Academy of Sciences in 2009. He also received his B. E. degree from Beijing University of Chemical Technology in 2000 and his LL. B. degree from Peking University in 2006. His research focuses on turbomachinery seal and CFD.